Composite Functional Materials
2025, 1(2): 20250203 https://doi.org/10.63823/20250203

Supplemental Information

Photocatalytic H_2O_2 production over $Ti(HPO_4)_2$ S-scheme heterojunction through push-pull electronic effects enhance the oxygen reduction

Shanyue He[a], Xin Zhang[a], Mei Chen[a], Hongquan Jiang[a,*], Yang Qu[b,*], Yanduo Liu[a,*], Jizhou Jiang[c,*]

a. School of Chemistry and Chemical Engineering, Harbin Normal University, Harbin 150025, P. R. China
b. Key Laboratory of Functional Inorganic Materials Chemistry (Ministry of Education), School of Chemistry and Materials Science, International Joint Research Center for Catalytic Technology, Heilongjiang University, Harbin 150080, P. R. China
c. School of Materials Science and Engineering, State Key Laboratory of Green and Efficient Development of Phosphorus Resources, Engineering Research Center of Phosphorus Resources Development and Utilization of Ministry of Education, Key Laboratory of Green Chemical Engineering Process of Ministry of Education, Hubei Key Laboratory of Plasma Chemistry and Advanced Materials, Novel Catalytic Materials of Hubei Engineering Research Center, Wuhan Institute of Technology, Wuhan 430205, P. R. China.

Characterization techniques

A Bruker D8 Advance diffractometer was used to analyze the X-ray powder diffraction (XRD) using Cu Kα radiation.

A Model Shimadzu UV-2750 spectrophotometer was adopted to record the UV-vis diffuse reflectance spectrum (DRS) by using with $BaSO_4$ as a reference.

Morphologies of samples were observed by using a scanning electron microscope (SEM, HitachiS-4800 instrument, Tokyo, Japan) and Transmission electron microscopy (TEM, JEOL JEM-2010EX instrument), operating at acceleration voltage of 15 kV and a 200 kV accelerating voltage, respectively.

A self-built equipment was applied to detect the steady-state surface photovoltage spectroscopy (SS-SPS), equipped with a lock-in amplifier (SR830, USA) synchronized with a light chopper (SR540, USA).

A Kratos-Axis Ultra DLD apparatus with an Al (mono) X-ray source was used to measure the X-ray photoelectron spectroscopy (XPS). All the XPS spectra were calibrated according to the C 1s peak at 284.8 eV.

The Inductive Coupled Plasma Optical Emission Spectroscopy (ICP-OES) was used to determine the optimal doping ratios of W in TPO_v samples. Samples were dissolved in hot HNO_3 medium prior to analyses by an Agilent 5800 ICP-OES instrument.

The electron paramagnetic resonance (EPR) measurements were carried out on a Bruker EMX plus model

Received: February 11, 2025. **Revised:** May 5, 2025. **Accepted:** May 10, 2025. **Available online:** December 10, 2025
***Corresponding author:** liuyd0608@163.com (Yanduo Liu), h.q.jiang1119@163.com (Hongquan Jiang), quyang@hlju.edu.cn (Yang Qu), 027wit@163.com (Jizhou Jiang).

spectrometer operating at the X-band frequency.

The near ambient pressure (NAP)-XPS spectra were collected at the SPECS NAP-XPS. The light irradiation was introduced into the analysis chamber through an observation window using a 300 W xenon lamp.

The time-resolved surface photovoltage (TR-SPV) measurements were tested by self-built experimental equipment, equipped with a second harmonic Nd: YAG laser (Lab-130-10H, Newport, Co.), high energy pyroelectric sensor (PE50BF-DIF-C, Ophir Photonics Group) and 1GHz digital phosphor oscilloscope (DPO 4104B, Tektronix).

The fs-TAS data was collected on a transient absorption spectrometer with a MIRA900 ultrafast laser system (Coherent, Inc., USA). The probe light was generated by focusing light at 800 nm through a sapphire crystal (modelocked Ti). After the pharos femtosecond laser pump to generate the 320 nm excitation pulse, the produced transient absorption spectroscopies were recorded at 350-700 nm with the time resolution of 150 fs.

The work function was tested by Scanning Kelvin probe (SKP) (SKP5050 system, Scotland). Samples were pressed into thin disk using a tablet press. The diameter was about 15 mm. Gold was used as a probe. The probe oscillation frequency was fixed at 78.0 Hz. The backing potential was set in the range of +7000 Mv to -7000 Mv. Data acquisition rate was kept at 13500 Hz. The disk was stuck with copper conducting resin upon the aluminum pallet. A working function measurement of 10 x 10 mapping was scanned with a step of 40 μm.

Evaluation for O_2 temperature programmed desorption

O_2-temperature programmed desorption (O_2-TPD) were performed by Chemisorption Analyzer, TP 5080 Chemisorb with a thermal conductivity detector (TCD). 50mg sample was preheated at 300 °C for 0.5 h to remove the other adsorbed gases and water and then cooled down to 30 °C under He flow rate of 30 mL/min The pure O_2 gas was introduced at 30 °C under O_2 flow rate of 50 mL/min for 0.5 h. The excess weak physically adsorbed O_2 was removed by He flow rate of 30 mL/min at 30 °C for 60 min. Then the temperature was increased to 700 °C with the heating rate of 10 °C/min under He flow rate of 30 mL/min.

Photoelectrochemical measurement

Using a conventional electrochemical workstation that had a standard three-electrode electro-chemical system tested the photoelectrochemical measurements (CHI760E, Shanghai). The film electrode was fabricated as follows: 50 mg of photocatalyst and 35 mL of terpineol were stirred vigorously to prepare the experimental electrode. Then, the mixture was coated onto the FTO electrode and then calcined at 200 °C for 120 min. The working electrode, Pt plate and Ag/AgCl electrode were taken as the working electrode, the counter electrode and the reference electrode on a LK2006 A workstation, respectively. 1 M KOH solution was used as electrolyte and a 300W Xenon lamp (wavelength range: 320-780 nm, spot diameter: 60 mm, light power: 134 mW/cm^2) with a 420 nm cut off filter was used as light source.

The transfer electron number (n) and H_2O_2 selectivity in the oxygen reduction reaction are determined by a rotating ring-disk electrode (RRDE). The test uses a three-electrode system: the disk electrode is loaded with the

sample, the ring electrode is usually made of platinum or gold, Hg/HgO serves as the reference electrode, Pt/C as the counter electrode, and the electrolyte is a saturated oxygen 0.1 M KOH solution. The RRDE speed is set at 1600 rpm, with a potential range of 0 -1.0 V vs. RHE. Transfer electron number *n*:

$n = 4I_d/(I_d+I_r/N)$

H_2O_2 selectivity:

Selectivity (%)=$200\times(I_r/N)/(I_d+I_r/N)$

where I_r is the ring current, I_d the disk current, and N the collection efficiency (N=0.35).

Hydroxyl radical amount measurement

0.05 g of the sample was dispersed in 60 mL of 1×10^{-3} mol L^{-1} aqueous solution in a quartz reactor. The suspension was stirred for 30 min before irradiation. After a given irradiation time with a spectrofluorometer (PerkinElmer LS 55), a certain amount of the solution was transferred into a Pyrex glass cell for the fluorescence measurement of 7-hydroxycoumarin with characteristic emission peak at about 460 nm under the light excitation of 332 nm.

Electron paramagnetic resonance

The electron paramagnetic resonance (EPR) tests of free radicals were carried out on the Bruker EMX plus model spectrometer. The preparation process of DMPO reserve solution is as follows: Under dark conditions, take 4 mL of high-purity water (or anhydrous methanol) and place it in a brown clamp bottle. Introduce high-purity nitrogen gas for 30 minutes to remove dissolved oxygen from the high-purity water (or anhydrous methanol). Quickly add 0.2263 g of DMPO solid and seal the clamp bottle. Continue to introduce high-purity nitrogen gas for deoxygenation and ventilation for more than 20 minutes to prepare a 0.5 mol/L DMPO reserve solution. Store it in a refrigerator in the dark and freeze it. Dilute it 10 times before use. The electron paramagnetic resonance testing process for free radical scavengers is as follows: inject a catalyst suspension with a volume of 50 μ L and a concentration of 4.000 g/L into 500 μ L of a specific scavenger solution with a concentration of 50 mmol/L (DMPO high-purity water or anhydrous methanol solution, DMPO high-purity water solution is used to detect ·OH, DMPO methanol solution is used to detect $\cdot O_2$-). After mixing evenly, transfer the mixture into a capillary column, seal it with vacuum grease, and then transfer it into a quartz sample tube. Place the quartz sample tube in the resonance chamber of an electron spin resonance spectrometer, and use a 150 W xenon lamp as the experimental light source to irradiate the reaction for a certain period of time before detection.

In-situ DRIFTS measurements

The *in-situ* diffuse reflectance infrared Fourier transform spectroscopy (DRIFTS) analysis was carried out in an *in-situ* diffuse reflectance pool with a Bruker Vector FTIR spectrometer (6700) and MCT detector which was cooled by liquid N_2. Firstly, a certain amount of KBr was filled into the reaction cell, and then covered with 0.2 g catalyst. The reaction cell was placed in the test chamber and heated to 175 °C under N_2 flow for 30 min to remove adsorbed impurities and then cooled to room temperature. In order to simulate the photocatalytic H_2O_2 production process, the

O_2 and H_2O were passed into the reaction cell. In this condition, a certain amount of O_2 and H_2O could be adsorbed on the surface of sample and then purged with N_2. Subsequently, the sample was irradiated under visible light. A 300 W Xenon arc lamp was used as the light source.

Theoretical calculations

The Vienna Ab Initio Package (VASP) was employed to perform all the density functional theory (DFT) calculations within the generalized gradient approximation (GGA) using the Perdew, Burke, and Enzerhof (PBE) formulation.[S1-3] The projected augmented wave (PAW) potentials were applied to describe the ionic cores and take valence electrons into account using a plane wave basis set with a kinetic energy cutoff of 450 eV.[S4, S5] Partial occupancies of the Kohn-Sham orbitals were allowed using the Gaussian smearing method and a width of 0.05 eV. The electronic energy was considered self-consistent when the energy change was smaller than 10^{-5} eV. A geometry optimization was considered convergent when the force change was smaller than 0.03 eV/Å. Grimme's DFT-D3 methodology was used to describe the dispersion interactions. [S6] The vacuum spacing perpendicular to the plane of the structure is 20 Å. The Brillouin zone integral utilized the surfaces structures of 2×2×1 monkhorst pack K-point sampling. The Charge density difference of system: $\Delta\rho = \rho total - \rho A - \rho B$, where ρtotal is the charge density of Binding systems, ρA and ρB is the sub charge density. Finally, the adsorption energies (Eads) were calculated as Eads= Ead/sub -Ead -Esub, where Ead/sub, Ead, and Esub are the total energies of the optimized adsorbate/substrate system, the adsorbate in the structure, and the clean substrate, respectively.

Evaluation of photoactivities

The photocatalytic H_2O_2 production test system is self-built. The test procedure is as follows: disperse 20 mg of catalyst powder in 20 mL of deionized water, transfer it to a custom-made quartz reactor, and keep the entire reaction process under continuous stirring. First, in the dark, maintain the system for 30 min while continuously bubbling O_2 to ensure the catalyst is fully saturated with O_2. Then, carry out the reaction under visible light irradiation for 1 h. The light source is a 300 W xenon lamp, providing an average light intensity of 50 mW/cm². Every 15 min, use a syringe to withdraw 1.5 mL of the reaction solution from the reactor. After filtering out the catalyst with a membrane filter to obtain a clear solution, determine the H_2O_2 content using the iodometric method and quantitatively analyze the H_2O_2 yield with a UV-visible absorption spectrophotometer.

Iodometric determination of H_2O_2 content: Add 0.5 mL of 0.4 mol/L KI solution and 0.5 mL of 0.1 mol/L potassium hydrogen phthalate ($C_8H_5KO_4$) solution to the reaction solution obtained by filtration. Mix well and maintain for 50 minutes. The iodometric principle is based on the reaction of H_2O_2 with I^- in acidic conditions to form I_3^- ($H_2O_2+3I^-+2H^+ \rightarrow I_3^-+2H_2O$), which has a strong absorption at around 350 nm. Measure the absorbance at 350 nm to determine the I_3^- content, and thus calculate the total amount of H_2O_2 produced in the reaction.

Scavenger experiments: To explore the effects of different scavengers on H_2O_2 generation activity under the same conditions and investigate the H_2O_2 generation pathway, prepare solutions of benzoquinone (BQ), tert-

butylalcohol (TBA), ethylenediaminetetraacetic acid disodium salt (EDTA-2Na), and Potassium dichromate ($K_2Cr_2O_7$) at a concentration of 1 mM. Add 20 mg of catalyst and 20 mL of a mixed solution of water and scavenger to the reaction system to maintain a concentration of 1 g/L. Conduct performance tests under visible light. To compare the effects of Ar and O_2 on photocatalytic H_2O_2 generation activity, first continuously bubble nitrogen into the reaction solution in the dark for 60 min to ensure no residual O_2. Then, perform photocatalytic experiments under continuous Ar flow.

H_2O_2 decomposition experiments: Disperse a certain amount of catalyst in a 1 mM H_2O_2 solution. Under visible light irradiation, measure the H_2O_2 content to compare the effects of different samples on H_2O_2 decomposition.

Superoxide dismutase (SOD) experiments: Following literature reports, disperse 10 mg of catalyst uniformly in a mixed solution of 45 mL of phosphate buffer (1 mM, pH 7.4) and 5 mL of glycerol. Then add SOD solutions at different concentrations (0 μM, 0.5 μM, 1 μM, and 2 μM). After uniform dispersion and dark adsorption, irradiate light for 2 min, and then take samples to measure and calculate the H_2O_2 concentration.

Solar-to-Chemical Conversion (SCC) Testing: In the reaction system, the photocatalyst concentration is 5 g/L (disperse 150 mg of catalyst powder in 30 mL of deionized water). The SCC test is performed under pure water conditions and AM 1.5G illumination. Solar-to-Chemical Conversion Efficiency:

$$SCC=[\Delta G_{(H_2O_2)}\times n_{(H_2O_2)}/(I\times S\times T)]\times 100\%$$

where $\Delta G_{(H_2O_2)}$, $n_{(H_2O_2)}$, I, S, and T represent the Gibbs free energy of H_2O_2 production (117 kJ/mol), the moles of H_2O_2 produced, the energy intensity of AM 1.5 G solar radiation (50 mW/cm²), the irradiated sample area, and the irradiation time, respectively.

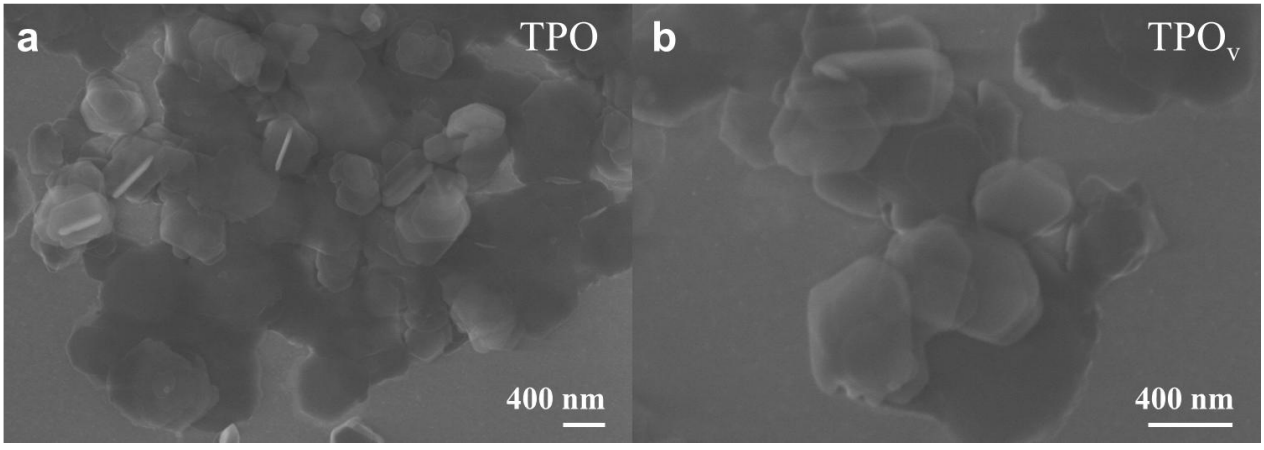

Figure S1. SEM images of investigated samples.

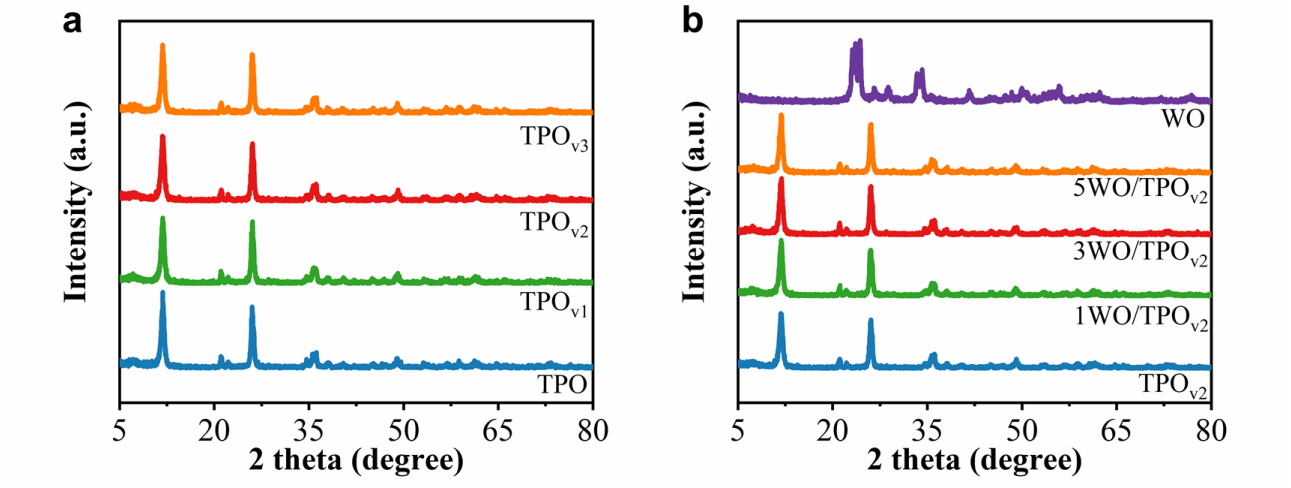

Figure S2. XRD patterns of the investigated samples.

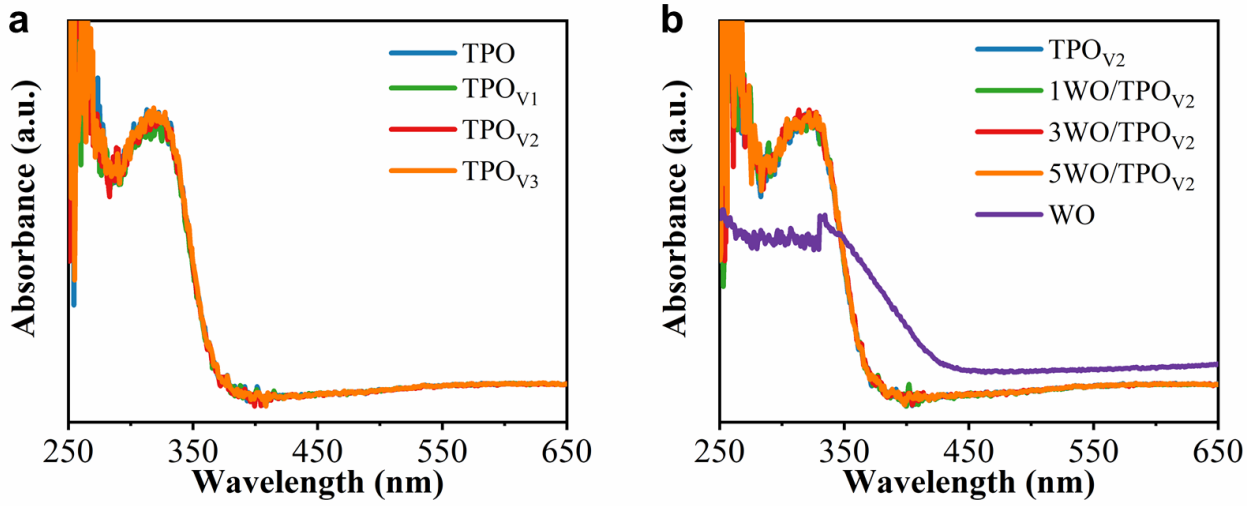

Figure S3. DRS spectra of the investigated samples.

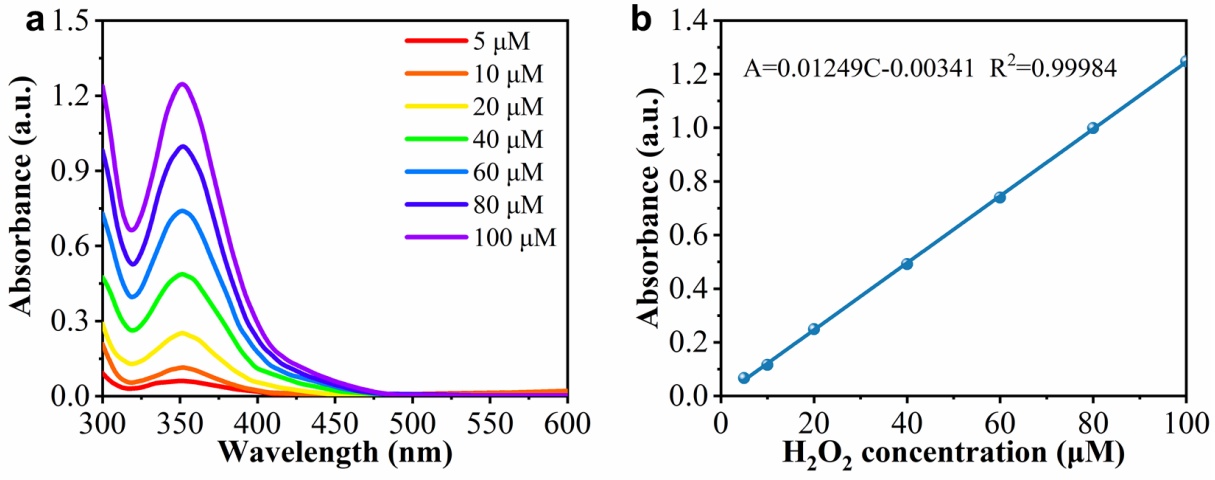

Figure S4. (a) Determination of the UV-Vis absorption intensity of different standard concentrations of H_2O_2 by the iodometric method. (b) The linear fitting formula for standard H_2O_2 concentration.

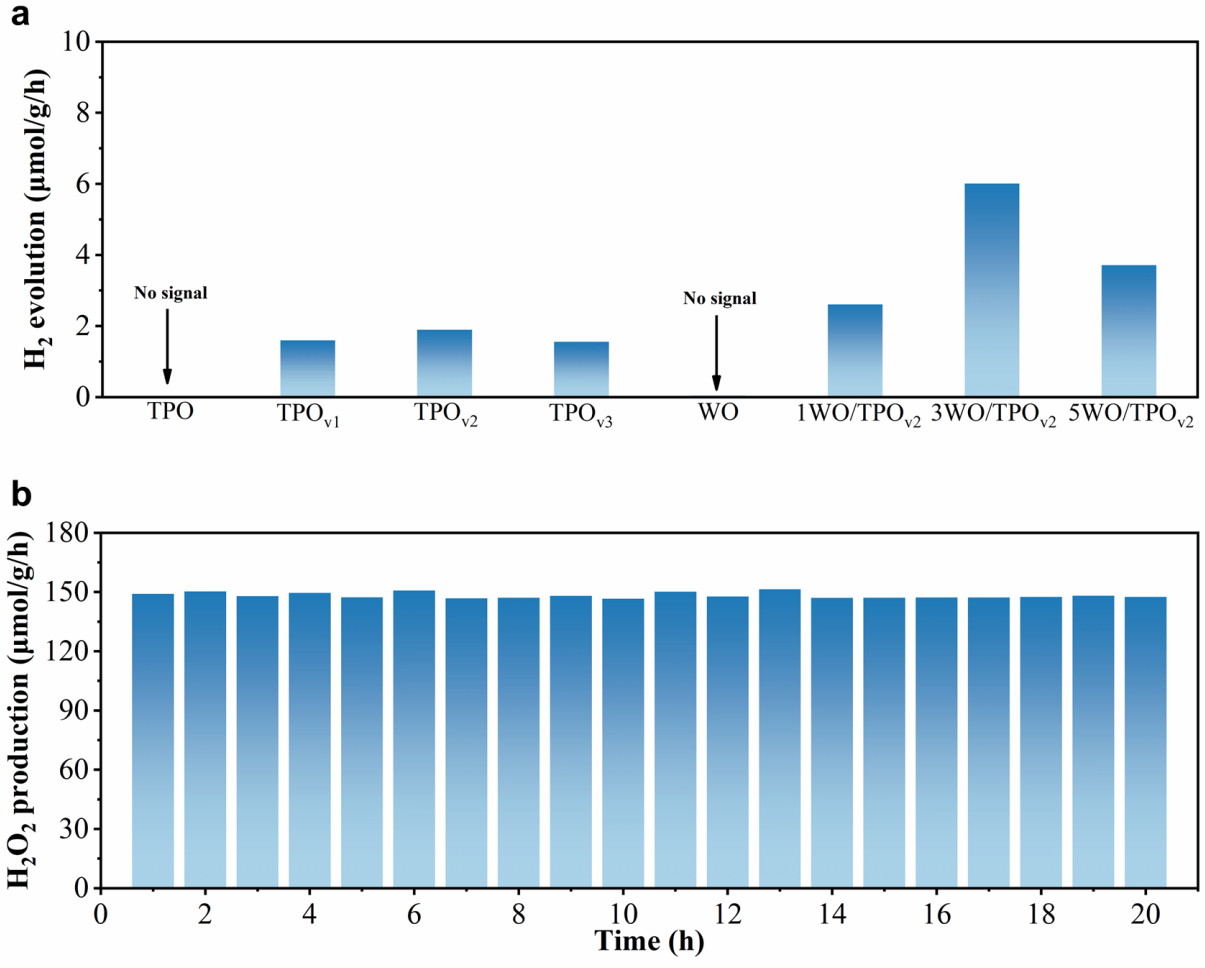

Figure S5. (a) Photocatalytic H_2 evolution rates of different samples. (b) Photocatalytic activity of H_2O_2 generation in the cyclic tests of advantage samples.

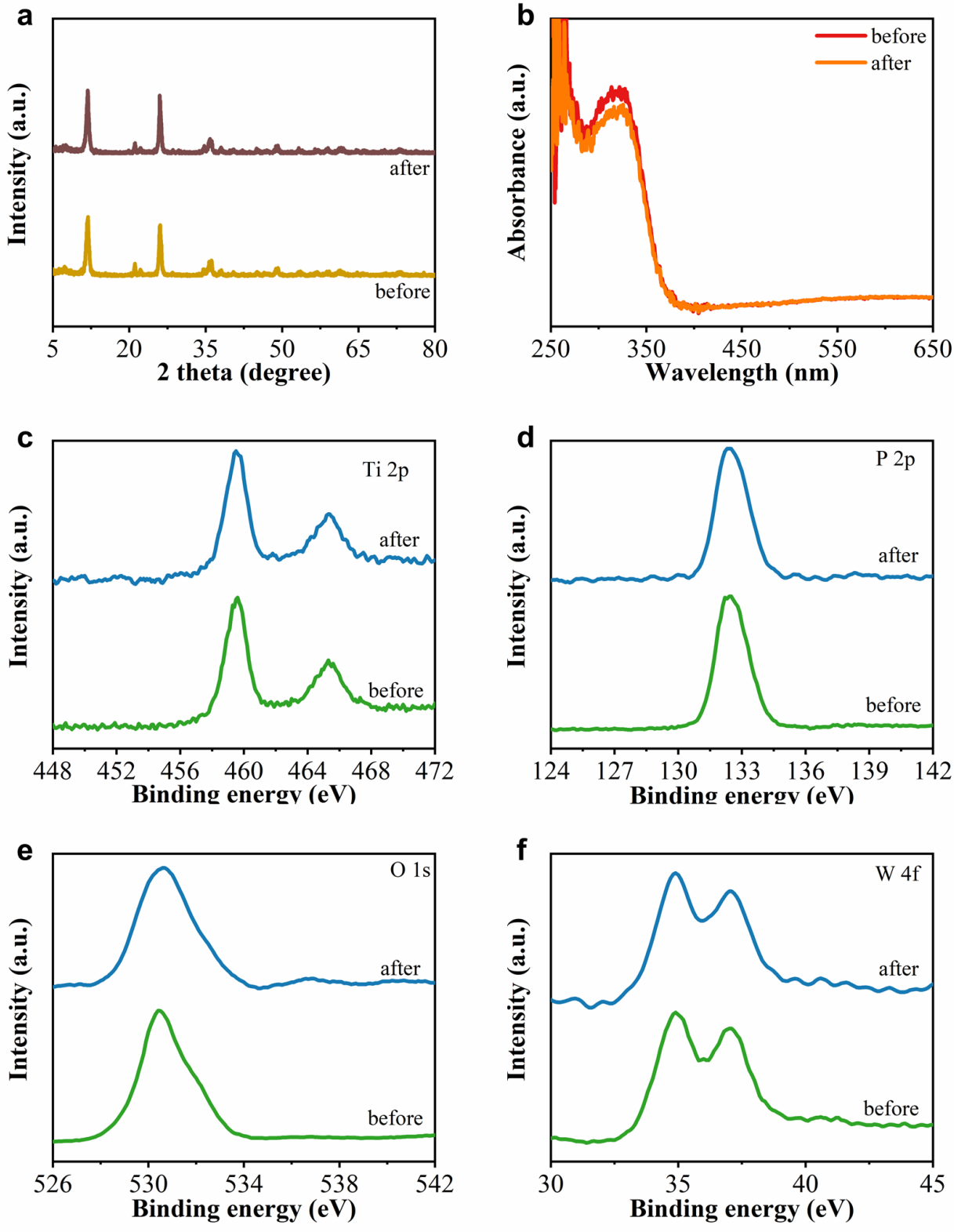

Figure S6. (a) XRD patterns, (b) UV-vis DRS spectra and (c-f) XPS analyses of advantage sample before and after reaction.

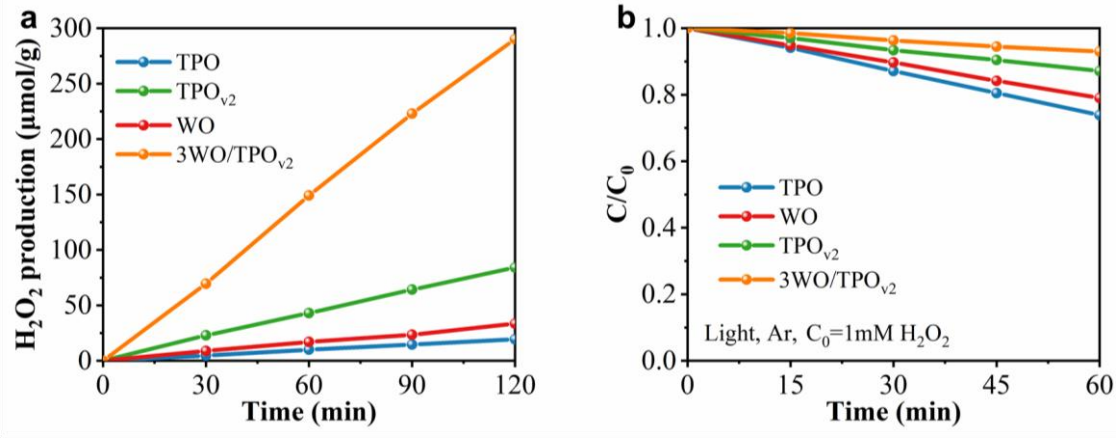

Figure S7. (a) Photocatalytic H_2O_2 generation rate of investigated samples. (b) H_2O_2 (1 mM) decomposition test of the investigated catalysts in N_2.

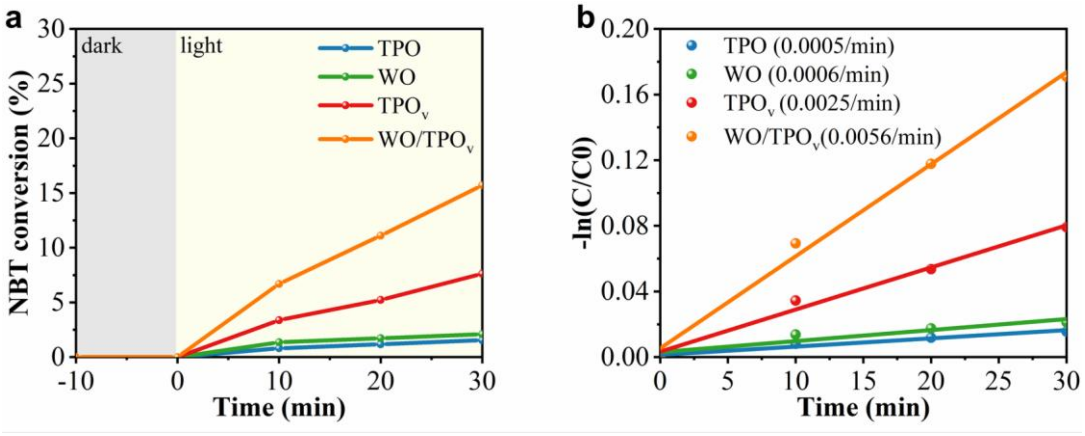

Figure S8. (a) Photodegradation of NBT by $\cdot O_2^-$ radicals generated over different photocatalysts. (b) The kinetic constant of photodegradation of NBT for $\cdot O_2^-$ radicals detection over different photocatalysts.

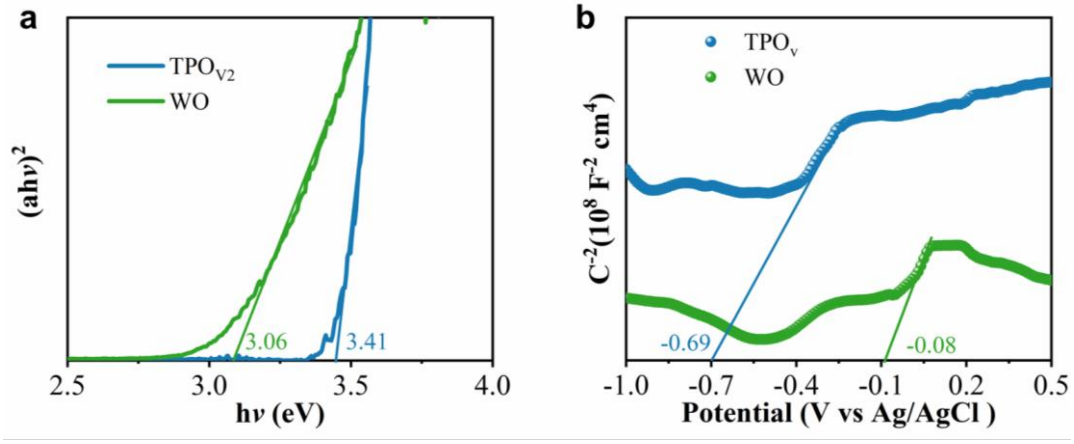

Figure S9. (a) Tauc plots and (b) Mott-Schottky plot schematic diagram of the position of investigated samples.

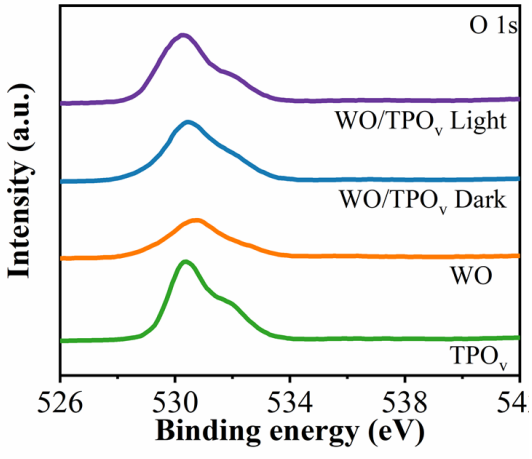

Figure S10. *In-situ* XPS analyses of O 1s over investigated samples.

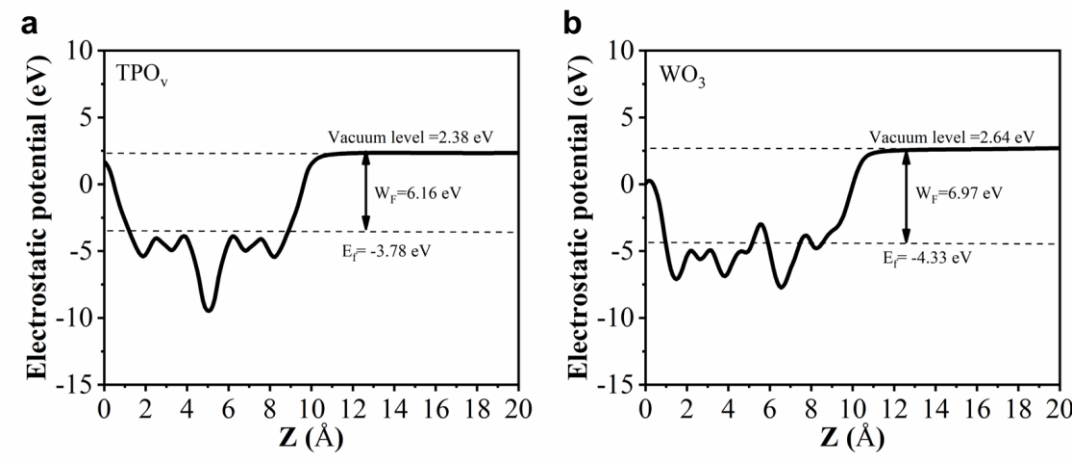

Figure S11. The calculated work function of investigated samples.

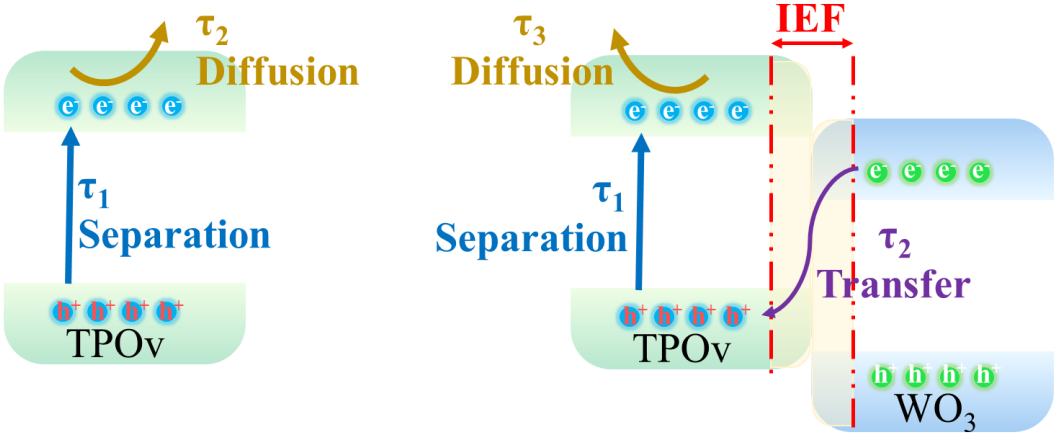

Figure S12. The proposed charge transfer and separation process of TPO$_v$ and WO/TPO$_v$.

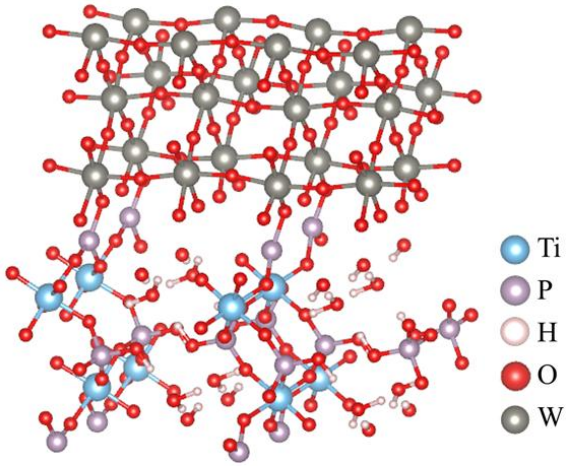

Figure S13. Schematic diagram of WO/TPO$_V$ heterojunction structure.

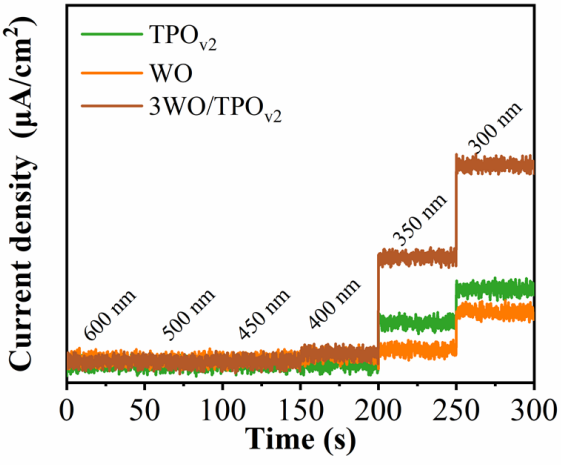

Figure S14. Photocurrent action spectra under different-wavelength light irradiation of investigated samples.

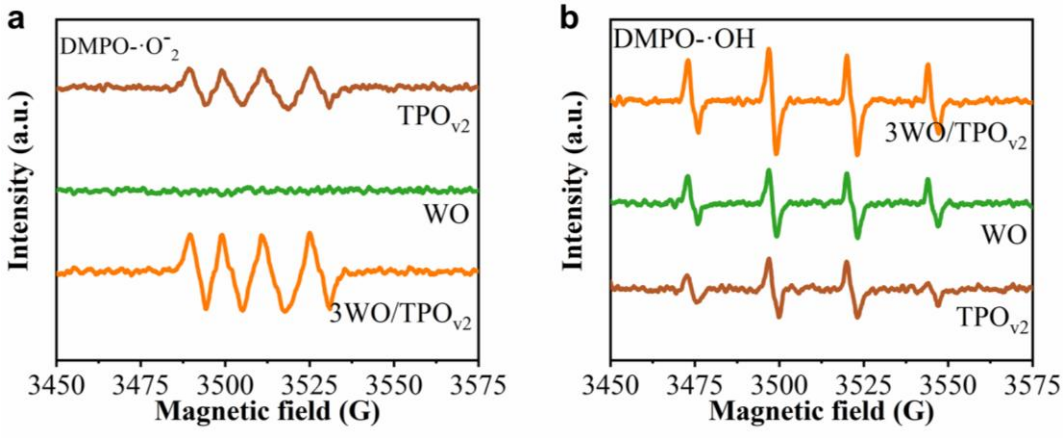

Figure S15. EPR spectra of (a) DMPO-·O_2^- and (b) DMPO-·OH species in aqueous solution produced over investigated samples.

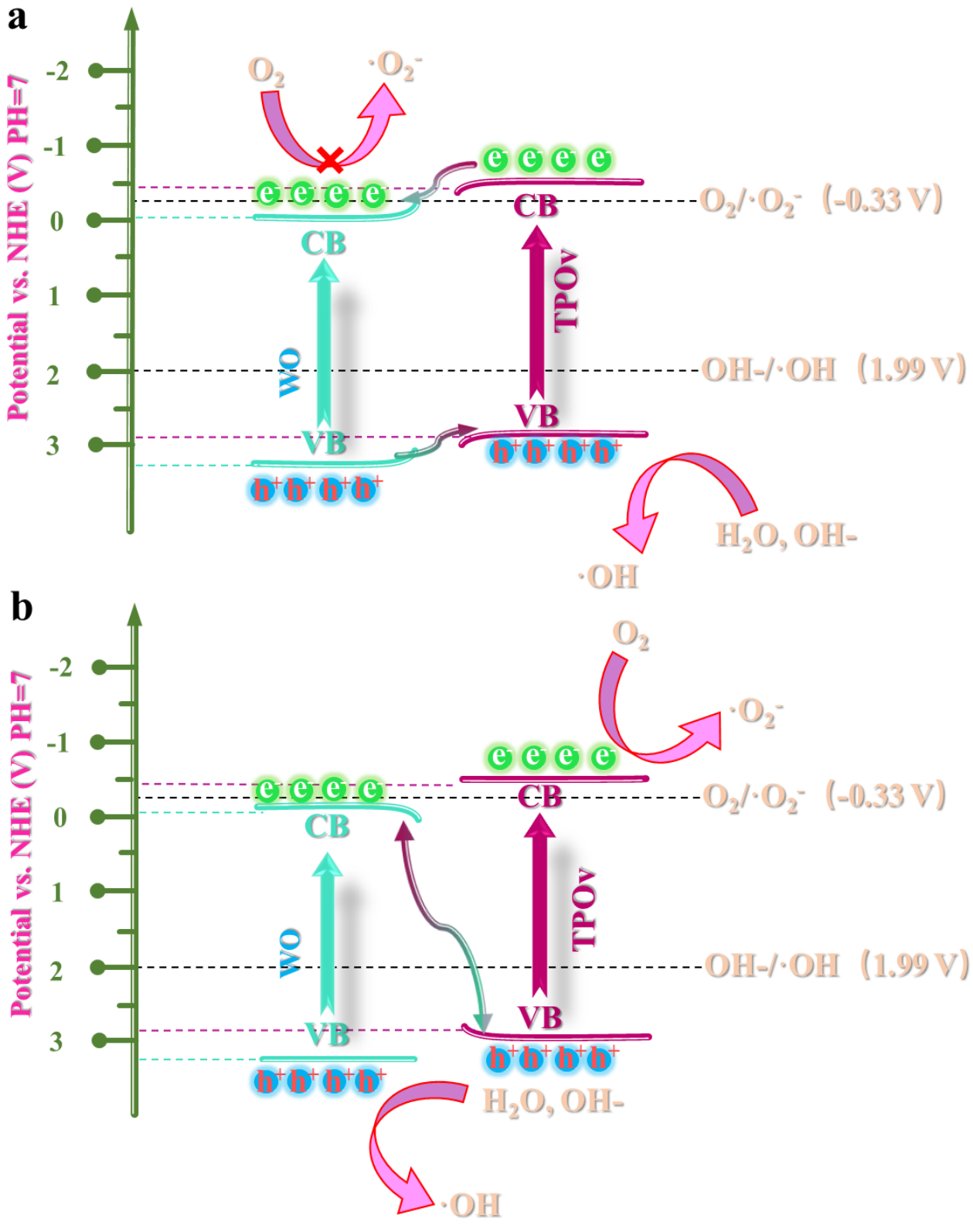

Figure S16. Schematic diagrams of (a) conventional II type and (b) S-scheme heterojunction corresponding to the DMPO adducts EPR results.

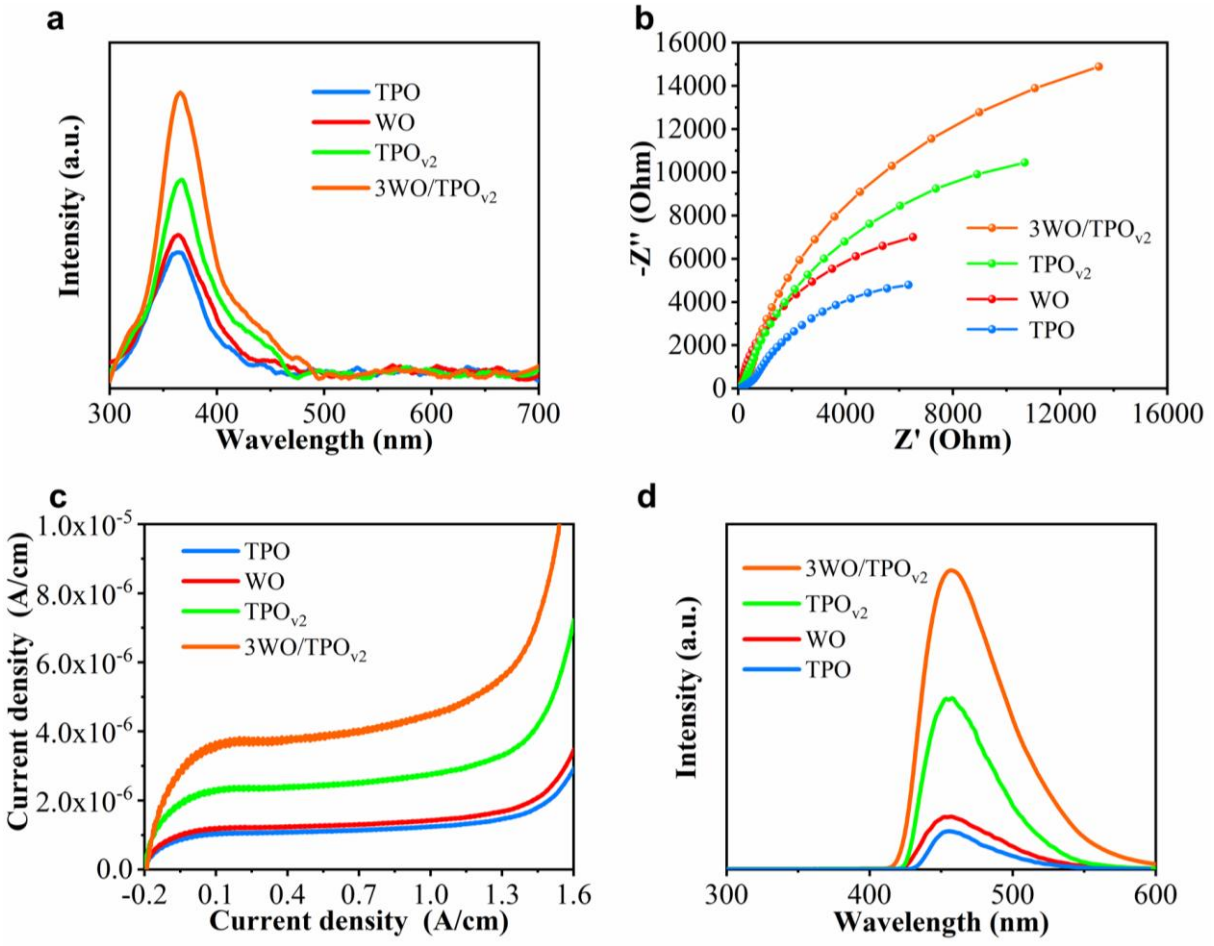

Figure S17. (a) SS-SPS spectra, (b) EIS spectra, (c) I-V curves under irradiation with UV-Vis light and (d) Fluorescence spectra related to the formed ·OH amounts of investigated samples.

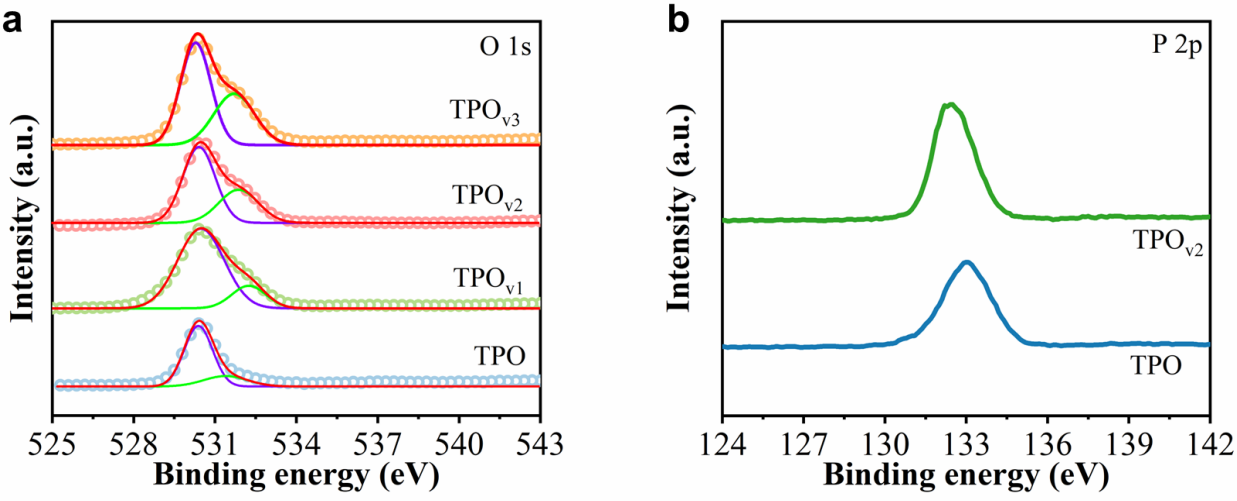

Figure S18. XPS analyses of (a) O1s and (b) p 2p over investigated samples.

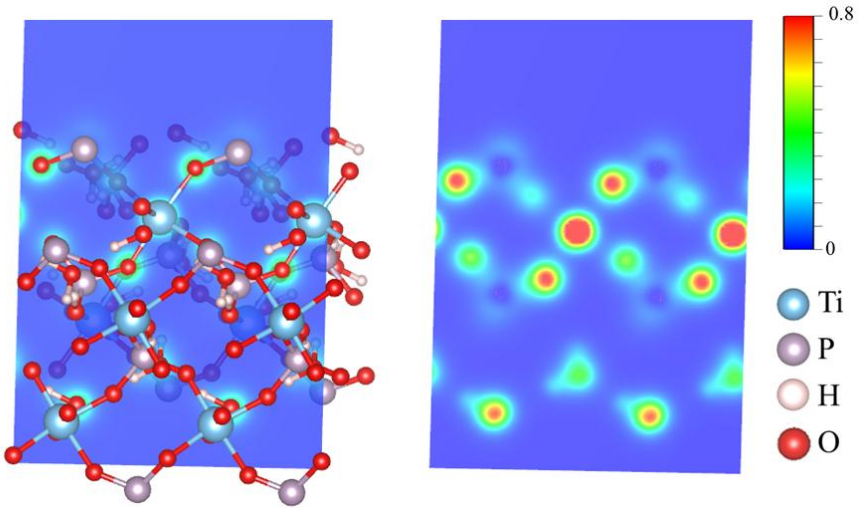

Figure S19. Local charge density map of TPO.

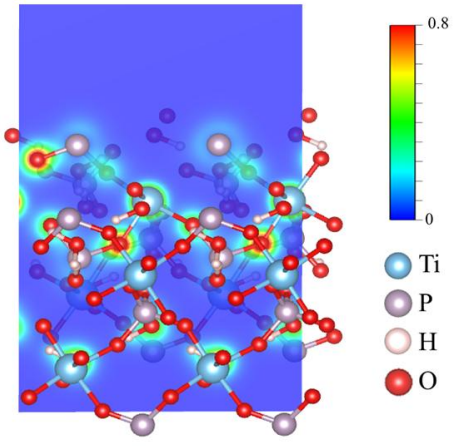

Figure S20. Local charge density map of TPO_v.

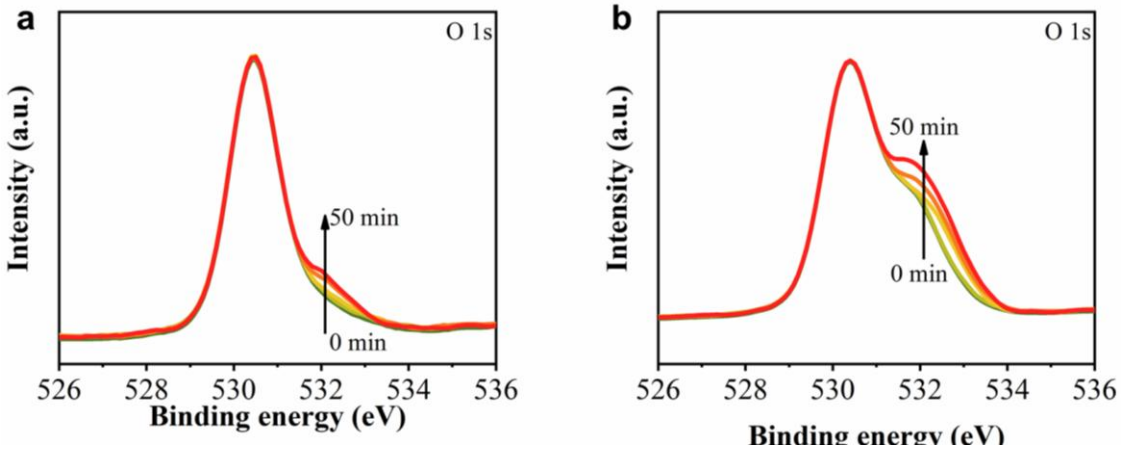

Figure S21. *In-situ* XPS analyses of O 1s over investigated samples.

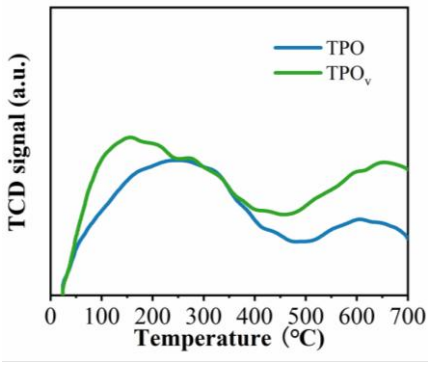

Figure S22. O_2-TPD curves of investigated samples.

From the perspective of desorption peak characteristics, which directly reflect the strength and type of O_2 adsorption, the O_2-TPD curve of the TPO_v material shows obvious differences from that of the TPO material in both the low-temperature physical adsorption region and the medium-high temperature chemical adsorption region.

In the low-temperature range (typically 50-300 °C, corresponding to physical adsorption), the TPO_v material exhibits a significantly stronger desorption peak intensity than the TPO material. Physical adsorption mainly relies on van der Waals forces between O_2 molecules and the material surface, and the peak intensity is positively correlated with the amount of physically adsorbed O_2. The higher peak intensity of TPO_v in this region indicates that its surface has more adsorption sites suitable for physical adsorption—this is likely due to the introduction of the Ti^{3+}-O_v-P structure, which modifies the surface morphology and electron distribution of the material, increasing the specific surface area and the number of weak interaction sites. In contrast, the TPO material without the Ti^{3+}-O_v-P structure has fewer physical adsorption sites, resulting in a weaker low-temperature desorption peak and a lower total amount of physically adsorbed O_2.

In the medium-high temperature range (typically 400-700 °C, corresponding to chemical adsorption), the difference between the two materials is more significant. Chemical adsorption is a process involving electron transfer or chemical bond formation between O_2 molecules and the material surface, and the position and intensity of the desorption peak are related to the strength of the chemical bond and the number of chemical adsorption sites. The TPO_v material shows a prominent desorption peak in the medium-temperature region. This indicates that the Ti^{3+}-Ov-P structure provides a large number of strong chemical adsorption sites: Ti^{3+}, as a low-valence titanium ion, has unpaired electrons that can form coordinate bonds with O_2 molecules; oxygen vacancies (O_v) act as electron traps to capture O_2 molecules and promote electron transfer from the material to O_2. In comparison, the TPO material only has a weak and broad desorption peak in the medium-high temperature range, which means that its chemical adsorption sites are not only scarce but also form relatively unstable chemical bonds with O_2 (requiring lower temperature to break the bonds for desorption).

In addition, the O_2-TPD curve of the TPO_v material does not show obvious tailing in either the physical or

chemical adsorption regions, while the TPO material has a slight tailing in the low-temperature chemical adsorption region. This phenomenon further confirms that the adsorption sites of the TPO_v material are more uniform (whether for physical or chemical adsorption), which is beneficial to the stable adsorption of O_2 molecules; while the TPO material has uneven adsorption site distribution, leading to inconsistent adsorption strength and thus peak tailing. Therefore, whether in terms of chemical adsorption or physical adsorption, the O_2 adsorption effect of the TPO_v material is significantly better than that of the TPO material.

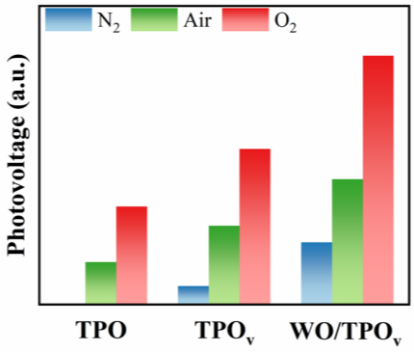

Figure S23. SS-SPS spectra in different atmospheres of investigated samples.

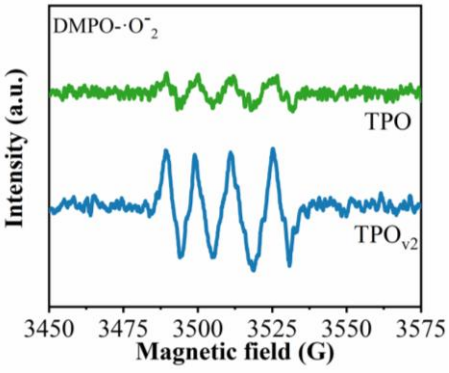

Figure S24. EPR spectra of DMPO-·O_2^- in aqueous solution produced over investigated samples.

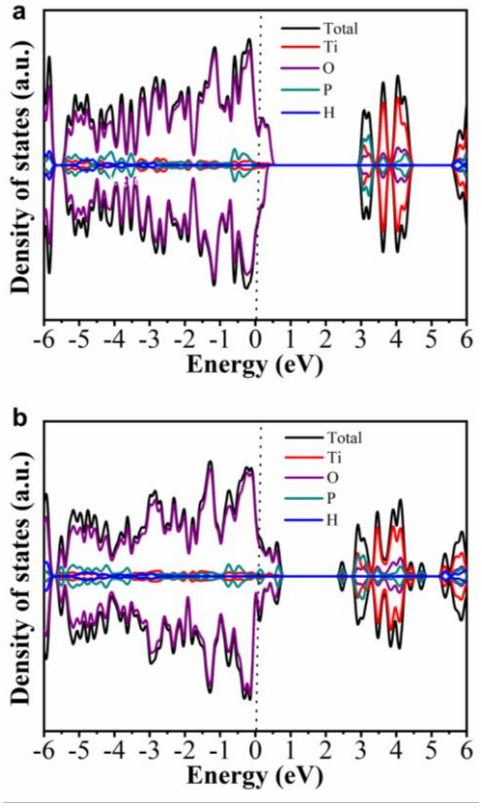

Figure S25. Projected density of states (PDOS) for (a) $Ti(HPO_4)_2$ and (b) TPO_{v2}.

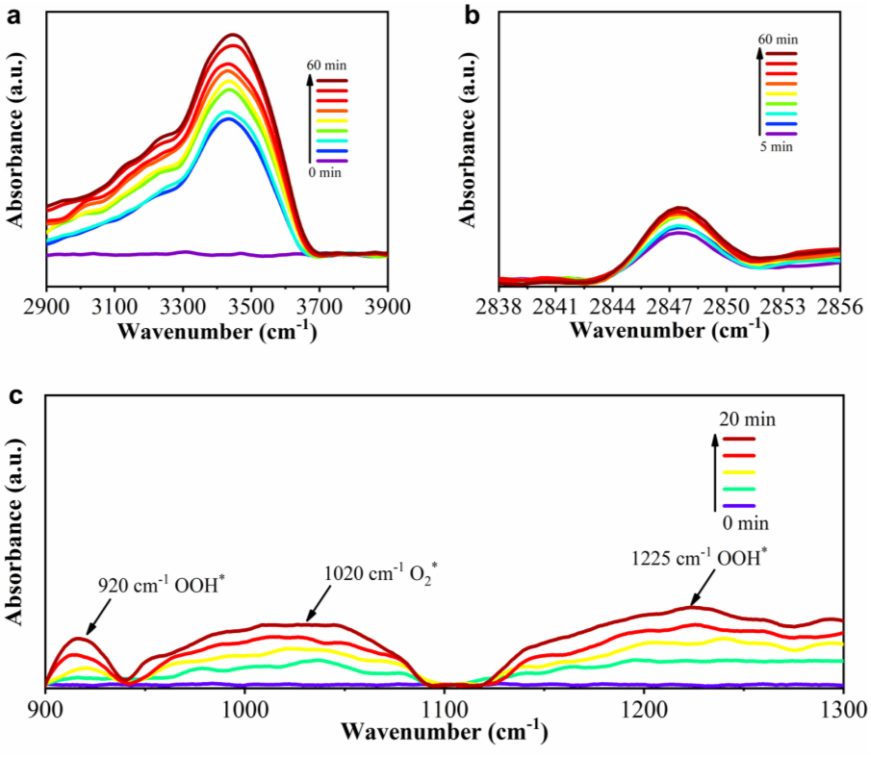

Figure S26. *In-situ* DRIFTS spectra of (a) H_2O_2 adsorption, (b) produced H_2O_2 and (c) H_2O conversion under light irradiation over TPO.

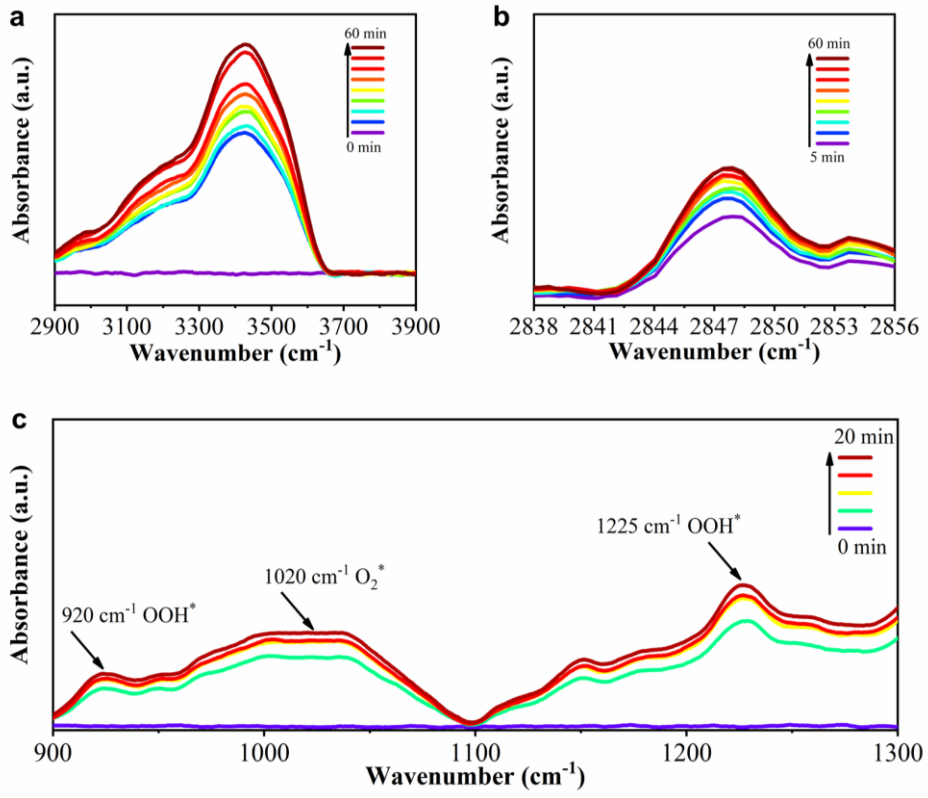

Figure S27. *In-situ* DRIFTS spectra of (a) H_2O_2 adsorption, (b) produced H_2O_2 and (c) H_2O conversion under light irradiation over TPO_v.

Table. S1. Comparison of recently reported photocatalysts with this work for photosynthetic H_2O_2.

Photocatalysts	Time (h)	Mass activity (μmol/g/h)	SCC (%)	Reaction conditions	Refs
APO/N-TPO	1	162	0.86	Solution volume: 20 mL; O_2 saturated pure water; Catalyst concentration: 1 g/L; Xe-lamp, AM 1.5 G, 50 mW/cm^2	This work
Cs_3PMo_{12}	1	76.5	0.50	Solution volume: 50 mL; O_2 saturated pure water; Catalyst concentration: 0.5 g/L; Xe-lamp, AM 1.5 G, 450 mW/cm^2	S7
$BO_{0.5}$-CN	1	114.7	0.25	Solution volume: 20 mL; O_2 saturated pure water; Catalyst concentration: 7.5 g/L; Xe-lamp, AM 1.5 G, 100 mW/cm^2	S8
COF-2CN	2	1601	0.60	Solution volume: 2 mL; O_2 saturated pure water; Catalyst concentration: 1.5 g/L; Xe-lamp, ≥420, 100 mW/cm^2	S9
SO_3H-COF	1	135.6	0.40	Solution volume: 50 mL; O_2 saturated pure water; Catalyst concentration: 0.9 g L−1; Xe-lamp, AM 1.5 G 100 mW/cm^2	S10
TpDz	1	7327	0.62	Solution volume: 20 mL;	S11

Photocatalysts	Time (h)	Mass activity (μmol/g/h)	SCC (%)	Reaction conditions	Refs
RF-CN-bm	12	17.4	0.50	O_2 saturated pure water; Catalyst concentration: 0.17 g/L; Xe-lamp, ≥420, 300 W Solution volume: 30 mL; O_2 saturated pure water; Catalyst concentration: 1.67 g/L; Xe-lamp, AM1.5G, 35.2 mW/cm^2	S12
CNIO-GaSA	1	331.7	0.40	Solution volume: 50 mL; O_2 saturated pure water; Catalyst concentration: 1 g/L; Xe-lamp, ≥420, 100 mW/cm^2	S13
COF-TfpBpy	1	46.8	0.57	Solution volume: 400 mL; O_2 saturated pure water; Catalyst concentration: 1.5 g/L Xe-lamp, AM 1.5 G, 50 mW/cm^2	S14
Sb-SPC15	2	91.2	0.61	Solution volume: 50 mL; O_2 saturated pure water; Catalyst concentration: 1 g L−1; Xe-lamp, ≥420, 30.3 mW/cm^2	S15
PEI/CN	1	208.1	0.05	Solution volume: 20 mL; O_2 saturated pure water; Catalyst concentration: 1 g/L; Xe-lamp, ≥420, 40.8 mW/cm^2	S16
CTF-BDDBN	24	97.2	0.14	Solution volume: 50 mL; O_2 saturated pure water; Catalyst concentration: 0.6 g/L; Xe-lamp, ≥420, 44.5 mW/cm^2	S17
RF523	24	82.5	0.50	Solution volume: 30 mL; O_2 saturated pure water; Catalyst concentration:1.67 g/L; Simulated AM 1.5G: 400 mW/cm^2	S18
CN/PDI/rGO	24	24.2	0.20	Solution volume: 30 mL; O_2 saturated pure water; Catalyst concentration:1.67 g/L; Xe-lamp 420−500 nm, 43.3 mW/cm^2	S19

References

[S1] G. Kresse, J. Phys. Rev. B 1996, 54, 11169-11186.

[S2] J. Perdew, K. Burke, M. Ernzerhof, Phys. Rev. Lett. 1996, 77, 3865-3868.

[S3] G. Kresse, D. Joubert, Phys. Rev. B 1999, 59, 1758-1775.

[S4] P. Blöchl, Phys. Rev. B 1994, 50, 17953-17979.

[S5] S. Grimme, J. Antony, S. Ehrlich, H. Krieg, J. Chem. Phys. 2010, 132, 154104.

[S6] G. Henkelman, B. Uberuaga, H. Jonsson, J. Chem. Phys. 2000, 113, 9901.

[S7] C. W, Y. Zhang, Y. T. Qu, W. B. Hua, Z. X. Jia, J. B. Lu, G. Xie, J. M. Xiao, H. M. Hu, Y. Yang, J. Q. Liu, J. B. Bai, G. L. Xue, Small. 2024, 2401485.

[S8] Q. C. Chen, C. Ning, J. W. Fang, B. Y. Ping, G. Y. Li, L. Q. Kong, J. Y. Chen, Z. M. Sun, J. L. Wang, Q. S. Ruan, X. H. Niu, L. Tao, Chem. Eng. J. 2024, 487, 150581.

[S9] Y. H. Hou, P. Zhou, F. Y. Liu, Y. Y. Lu, H. Tan, Z. M. Li, M. P. Tong, J. R. Ni, Angew. Chem. Int. Ed. 2024, 63, e202318562.

[S10] L. Y. Li, X. M. Lv, Y. Y. Xue, H. B. Shao, G. F. Zheng, Q. Han, Angew. Chem. Int. Ed. 2024, 63, e202320218.

[S11] Q. B. Liao, Q. N. Sun, H. C. Xu, Y. D. Wang, Y. Xu, Z. Y. Li, J. W. Hu, D. Wang, H. J. Li, K. Xi, Angew. Chem. Int. Ed. 2023, 62, e202310556.

[S12] P. D. Su, J. K. Zhang, Y. H. Zhou, Z. Wei, S. Zhao, B. Yang, X. Zhao, J. Chen, Chem. Eng. J. 2023, 454, 140504.

[S13] H. Tan, P. Zhou, M. X. Liu, Q. H. Zhang, F. Y. Liu, H. Y. Guo, Y. Zhou, Y. Chen, L. Y. Zeng, L. Gu, Z. F. Zheng, M. P. Tong, S. J. Guo, Nat. Synthesis 2023, 2, 557-563.

[S14] M. P. Kou, Y. Y. Wang, Y. X. Xu, L. Q. Ye, Y. P. Huang, B. H. Jia, H. Li, J. Q. Ren, Y. Deng, J. H. Chen, Y. Zhou, K. Lei, L. Wang, W. Liu, H. W. Huang, T. Y. Ma, Angew. Chem. Int. Ed. 2022, 61, e202200413.

[S15] Z. Y. Teng, Q. T. Zhang, H. B. Yang, K. Kato, W. J. Yang, Y. R. Lu, S. X. Liu, C. Y. Wang, A. Yamakata, C. L. Su, B. Liu, T. Ohna, Nat. Catal. 2021, 4, 374-384.

[S16] X. K. Zeng, Y. Liu, Y. Kang, Q. Y. Li, Y. Xia, Y. L. Zhu, H. L. Hou, M. H. Uddin, T. R. Gengenbach, D. H. Xia, C. H. Sun, D. T. Mccarthy, A. Deletic, J. G. Yu, X. W. Zhang, ACS Catal. 2020, 10, 3697-3706.

[S17] L. Chen, L. Wang, Y. Y. Wan, Y. Zhang, Z. M. Qi, X. J. Wu, H. X. Xu, Adv. Mater. 2020, 32, 1904433.

[S18] Y. Shiraishi, T. Takii, T. Hagi, S. Mori, Y. Kofuji, Y. Kitagawa, S. Tanaka, S. Lchikawa, T. Hirai, Nat. Mater. 2019, 18, 985-993.

[S19] Y. Kofuji, Y. Isobe, Y. Shiraishi, H. Sakamoto, S. Tanaka, S. Lchikawa, T. Hirai, J. Am. Chem. Soc. 2016, 138, 10019-10025.